

$$M_0^\nu = \alpha^{-1} + f^{\nu-1}(L') + \epsilon \sum_{\mu=0}^{\nu-1} \bar{N}_\mu^{\nu-1} \mu! ,$$

$$M_\mu^\nu = \epsilon \bar{M}_{\mu-1}^{\nu-1} / \mu, \quad 1 \leq \mu \leq \nu$$

$$N_\mu^\nu = -\epsilon \sum_{\lambda=\mu}^{\nu-1} \bar{N}_\lambda^{\nu-1} \lambda! / \mu!, \quad 0 \leq \mu \leq \nu-1$$

$$\bar{M}_\mu^\nu = \delta \sum_{\lambda=\mu}^{\nu} (-1)^{\mu-\lambda} M_\lambda^\nu \lambda! / \mu!, \quad 0 \leq \mu \leq \nu$$

$$\bar{N}_0^\nu = -\alpha^{-1} + h^{\nu-1}(L') - \delta \sum_{\mu=0}^{\nu} (-1)^\mu M_\mu^\nu \mu! ,$$

$$\bar{N}_\mu^\nu = \delta N_{\mu-1}^\nu / \mu, \quad 1 \leq \mu \leq \nu .$$

We apologize for the opacity of this form. Nevertheless, it does allow more rapid calculation of numerical results than direct computer solution of the original set of equations. The final formulas for  $I$  and  $B$  may be written

$$I^\nu(x, y) = I_0 \theta(y) [f^\nu(y) + h^\nu(y)] / [f^\nu(x) + h^\nu(y)] ,$$

$$B^\nu(x, y) = a [h^{\nu-1}(x) - h^\nu(y)] / [f^\nu(x) + h^\nu(y)] .$$

\*Work partially supported by the U. S. Army Research Office, Durham, under Grant No. DA-ARO-D-31-124-6920 and the Joint Services Electronics Program (U. S. Army, Navy, and Air Force), under Grant No. AF-AFOSR-69-1622A.

<sup>1</sup>N. M. Kroll, *J. Appl. Phys.* **36**, 34 (1965).

<sup>2</sup>N. M. Kroll and P. L. Kelley (unpublished); C. S. Wang, *Phys. Rev.* **182**, 482 (1969).

<sup>3</sup>C. L. Tang, *J. Appl. Phys.* **37**, 2945 (1966).

<sup>4</sup>M. Maier, W. Kaiser, and J. A. Giordmaine, *Phys.*

*Rev.* **177**, 580 (1969); *Phys. Rev. Letters* **17**, 1275 (1966).

<sup>5</sup>E. E. Hagenlocker, R. W. Minck, and W. G. Rado, *Phys. Rev.* **154**, 226 (1967).

<sup>6</sup>See Wang, Ref. 2, and work cited therein.

<sup>7</sup>G. L. McAllister, M. M. Mann, and L. G. DeShazer, *IEEE J. Quantum Electron.* **QE-6**, 44 (1970).

<sup>8</sup>N. Bloembergen, G. Bret, P. Lallemand, A. Pine, and P. Simova, *IEEE J. Quantum Electron.* **QE-3**, 197 (1967).

## Filamentary Tracks Formed in Transparent Optical Glass by Laser Beam Self-Focusing. I. Experimental Investigation\*

George N. Steinberg

*Perkin-Elmer Corporation, Research Department, 50 Danbury Road, Wilton, Connecticut 06897*

(Received 14 January 1971)

The permanent damage in optical glass investigated here is characterized by filamentary tracks of fine fractures. These tracks are a few micrometers in diameter, straight to within 0.7  $\mu\text{m}$ , up to 9 cm long, and collinear with the incident laser beam. There may also be damage stars (regions of fracture gross compared with the track diameter). These damage stars are usually near the upstream ends of the tracks. Track formation is characterized by a flash of side-scattered white light from the track, laser light side-scattered from the damage stars, a marked increase in the exit divergence angle of the laser beam, and a weak back-scattered pulse of laser light. The back-scattered pulse preserves the polarization of the incident beam, is of shorter duration than the incident laser pulse, and has a frequency shift corresponding to Brillouin scattering from a free compressional sound wave in the glass. Track formation is accompanied by a detectable cylindrical sound wave. The track formation threshold is repeatable at different locations in the glass sample. Both the power threshold and the energy-density threshold are rapidly varying functions of the incident beam radius at focus. The threshold power is as low as 10 kW for a ruby-laser beam sharply focused in dense flint glass, and more than 2 MW for an unfocused beam in fused silica.

### INTRODUCTION

The type of filamentary track formation in glass we investigated was first reported by Hercher.<sup>1</sup> The experiments we performed established the threshold dependence on beam size for three types

of optical quality nonabsorbing glass. We found the threshold was repeatable in different glass samples of the same type, given the same incident beam conditions. We also investigated the characteristics of the many emissions accompanying track formation, and attempted to account for all

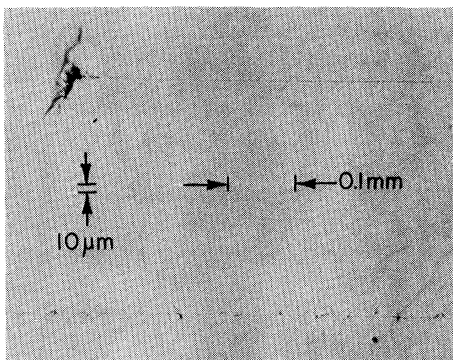


FIG. 1. Two typical filamentary tracks with damage stars.

significant beam energy losses.

APPARATUS AND MATERIALS TESTED

A Q-switched ruby laser was the source for all experiments. The ruby was a rod 0.635 cm in diam by 7.62 cm long, 0.05% Cr doped. Pumping was done at room temperature by a Trion Instruments TO-3000 Optical Maser Head with a 3000 J input from a ESU-150 energy storage unit and a PS-100 power supply. A Daly-Sims prism was placed between a 50% output mirror and the ruby to reduce the cavity Q for off-axis modes. The Q-switching was done by rotating a 99% reflectivity mirror at 15 000 rpm.

Under these conditions, the output consisted of

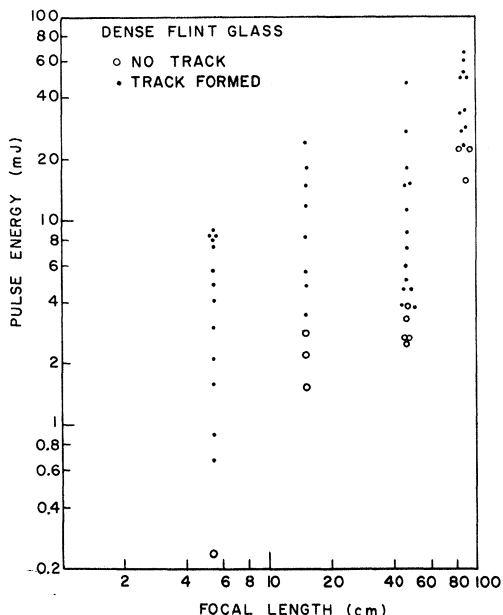


FIG. 2. Track formation data in dense flint glass.

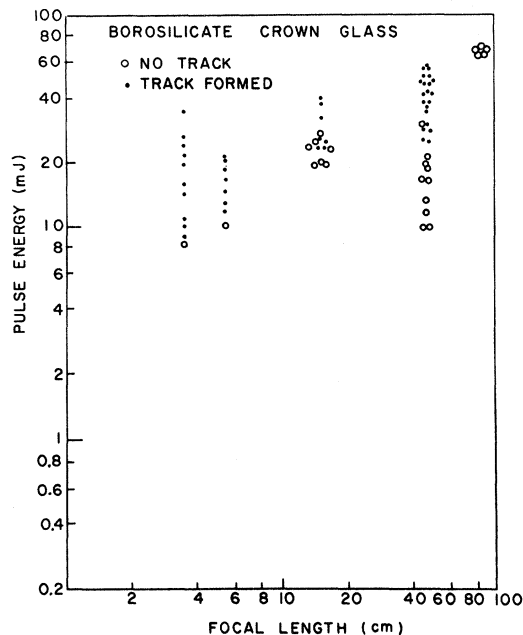


FIG. 3. Track formation data in borosilicate crown glass.

a 0.1-J pulse lasting 55 nsec. The over-all reproducibility was about 20% when a 10-min interval was allowed between pulses. The output beam passed through a variable attenuation cell containing copper sulfate in solution.

The attenuated output was sampled with beam splitters to measure the energy and shape of each pulse. Energy measurements were made on a calorimeter similar to the one described by Li and Sims.<sup>2</sup> The pulse shape was monitored with an RCA 7102 photomultiplier driving a Tektronics 585 oscilloscope.

Damage was caused by focusing the beam in a sample. Samples were 7.62 cm long and 0.635 cm thick. The beam passed through the length of the sample, and the sample was centered around the focus. Unless otherwise noted, a 46-cm focal lens was used. Beam diameter at the lens was 2 mm, which was 1.3 times the diffraction limit.

The majority of the tests were made on three types of optical glass selected for their range of properties. We used fused silica, borosilicate crown glass, and dense flint glass.

CHARACTERISTICS OF THE TRACKS

Figure 1 shows many of the track characteristics. A 1-MW 55-nsec (full width at half-maximum) ruby-laser pulse entered the borosilicate crown glass sample from the left. There is a region of planar cracking and discoloration which we term a rather large damage star. A track a few microns in diameter extends several millimeters downstream,

collinear with the laser beam. A second track, produced in another trial, is seen below the first.

The track occurs in the form of a cylindrical region of altered index of refraction, a micron or two in diameter, and up to several centimeters long in a straight line. The track always starts in a damage star, and it may disappear and then reappear, in the same straight line, although not necessarily at a damage star again. Eventually, the track disappears altogether, but the exit surface of the sample usually has a pit on the extended axis of the track. It was not possible to start a track at the entrance face of the sample, even when the beam was focused there. Typically, individual sections of a track are straight to within an rms deviation of one optical wavelength, and the entire track is straight to within 10 wavelengths.

The central core diameters of fused silica tracks were measured to range between 0.6 and 1.8  $\mu\text{m}$  and the dense flint glass, between 1.3 and 3.6  $\mu\text{m}$ .

Beam trapping or self-focusing must occur to explain the better than 1000 to 1 length to diameter ratio achieved in some of the tracks. Otherwise, the beam would spread by diffraction long before such a ratio could be established.

**THRESHOLD**

**Threshold as a Function of Focal Length**

The threshold required for track formation was determined for the three glasses as a function of the focal length of the external lens.

The data are plotted in Figs. 2-4. These figures contain data taken over a period of months on

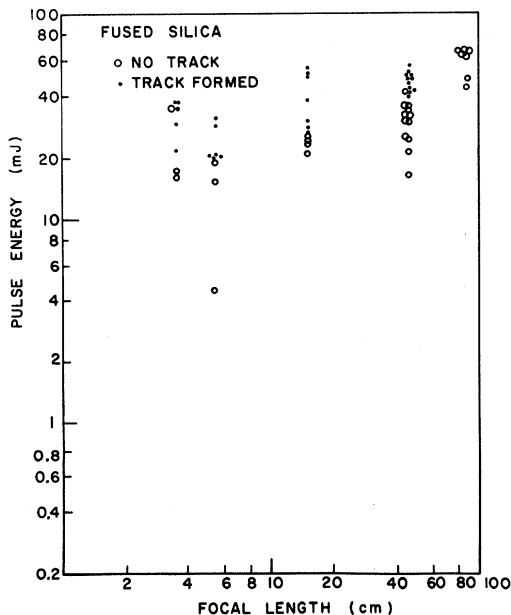


FIG. 4. Track formation data in fused silica.

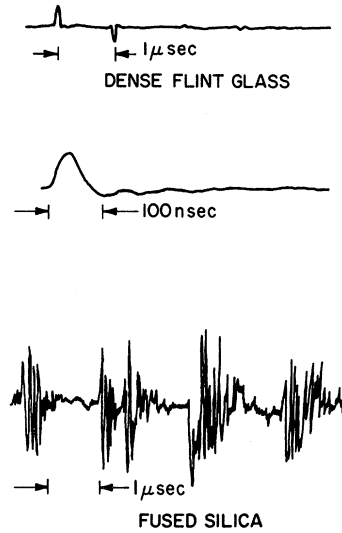


FIG. 5. Sound pulse amplitude accompanying track formation.

differing samples of the glasses. With few exceptions, the threshold is determined to within the reproducibility of the laser pulses. The sharpness and reproducibility indicate that track formation is not due to imperfections or impurities. The threshold is set by bulk properties of the material.

**Threshold as a Function of Pulse Duration**

We examined the effect of pulse duration on the track formation threshold energy by applying 38-nsec pulses as well as 55-nsec pulses to dense flint glass. The faster pulses were Q-switched with a cryptocyanine dye cell and the beam diameter was 1.4 mm at the external lens. The threshold for dense flint glass with a 5.4-cm lens was 1.8 mJ, or four times the threshold using the 55-nsec pulses and the 2-mm beam diameter. Tracks in borosilicate crown glass and fused silica could not be formed at all nor could they be formed in dense flint glass with the next longer focal length lens, within the power limits of the dye-cell Q-switched laser.

**Threshold with Beam Stop**

The track formation threshold was determined for fused silica when a stop was placed across part of the beam.

A 3/4-mm-wide stop was placed across the beam at a point where the beam diameter was 2 mm. About one-half the beam area, which included the center of the beam, was blocked out.

This raised the threshold to 1.7 times the previous value for the 15-cm lens. The threshold was not raised by the stop when a 3.5-cm lens was used.

TABLE I. Physical properties of the three test glasses.

Property	Fused silica	Borosilicate crown	Dense flint
Refractive index $n$ at 694.3 nm	1.45548	1.51324	1.75031
Density $\rho$ (kg/m <sup>3</sup> )	2200	2510	4720
Young's modulus $Y$ (GN/m <sup>2</sup> )	73.08	81.49	55.80
Modulus of rigidity $M$ (GN/m <sup>2</sup> )	31.16	33.73	22.36
Calculated compression wave speed $v$ (km/sec)	5.980	6.037	3.759
Measured sound speed (km/sec)	5.2	6.5	3.9

This experiment shows that the central region of the beam is not as effective as the periphery of the beam in forming tracks, especially in a more convergent beam.

#### DIRECT MEASUREMENT OF SOUND PULSES

We verified that track formation is accompanied by a sound pulse. The sound pulse was detected by an ultrasonic transducer in contact with the side of the sample under test. A phototube triggered the oscilloscope sweep. Typical oscilloscope recordings of these sound pulses are shown in Fig. 5. Borosilicate crown glass responds similarly to dense flint glass. The recording for fused silica is different from that for dense flint glass in two respects: The signal is much larger, and the first large pulse is preceded by two smaller pulses.

The recordings can be used to measure the speed of sound in the glass as follows. The first positive pulse is the sound that directly reaches the transducer and the second negative pulse is the sound that reaches the transducer after undergoing a re-

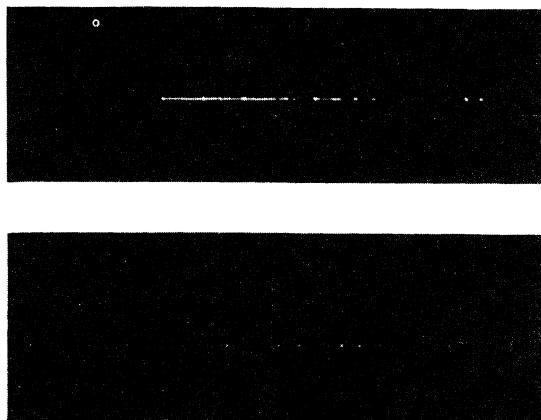


FIG. 6. Side-scattered white light (upper photo) and laser light (lower photo) during track formation. The laser pulse was incident from the left-hand side in each photo.

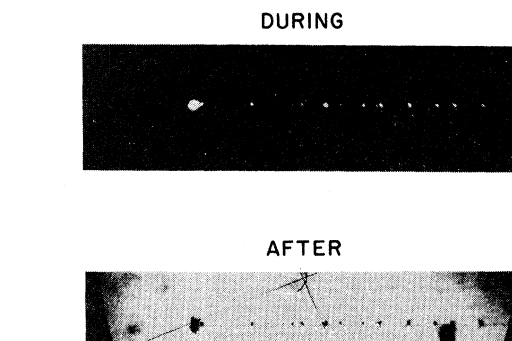


FIG. 7. Track photographs during (upper) and after (lower) formation. The laser pulse was incident from the left-hand side. The upper photo shows laser light only, as the side-scattered white light was blocked by a 694.3-nm spike filter. (Microscope cross hairs and dust in the lower photo should be ignored.)

flexion at the opposite face. The speed is computed by dividing the thickness of the sample by one-half the sum of the times required for the pulses to appear after the start of the sweep. The measured values may be compared with calculated values in Table I. The calculated values were found by evaluating the formula

$$v = \left( \frac{M}{\rho} \frac{4M - Y}{3M - Y} \right)^{1/2}$$

for the compression-wave speed  $v$ .

#### SIDE-SCATTERED LIGHT

During track formation, both white light and laser light are side scattered from the sample, as shown in Fig. 6. The track photograph made during the laser pulse (upper photograph, Fig. 7) shows blurred objects. These objects have a one-to-one

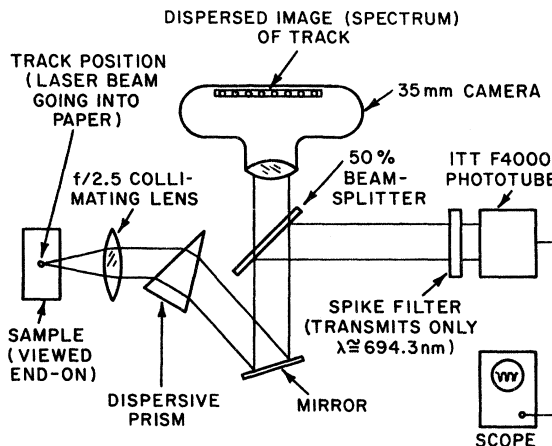


FIG. 8. Apparatus for simultaneously recording the spectrum and arrival time of side-scattered light.

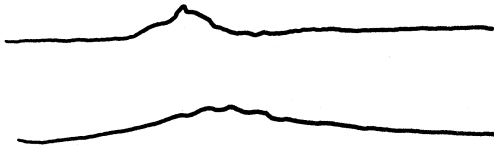


FIG. 9. Intensity of side-scattered laser light (upper trace) compared with a typical laser pulse. Time scale is 160 nsec over-all.

geometrical correspondence with the damage stars photographed later. We conjecture that the "during" photograph shows forming (i. e., expanding) fractures. The laser light that is side scattered from the sample is unpolarized independent of the plane of polarization of the incident light.

We built the apparatus of Fig. 8 to collect information on the spectrum of the side-scattered white light, and the arrival time of the laser light scattered by the damage stars. The scattered light is gathered over a wide angle by the  $f/2.5$  collimating lens. The light is then dispersed by a prism and sent partly to a 35-mm camera, and partly to an ITT F4000 phototube after a spike filter absorbs all but the laser light.

Typical data are shown in Figs. 9 and 10. Figure 9 shows the arrival time of the laser light side-scattered from fused silica. A typical output pulse is shown for comparison at the same sweep rate. The positions in the sample from which the laser light was scattered are shown in Fig. 10 as the horizontal row of white dots. The spectral distribution of the side-scattered white light is recorded as a vertical streak above the scattering points. The laser light is distinctly separate from the spectrum of the white light because the film sensitivity falls off rapidly at 640 nm.

The energy density at the focus of the 46-cm lens during these measurements was  $30.0 \text{ J/cm}^2 \pm 5\%$  for all the fused silica tests and  $29.6 \text{ J/cm}^2 \pm 5\%$  for all the borosilicate crown glass tests, respectively.

The dense flint glass scattered practically no laser light. Laser-light scattering was observed at only one point in 12 trials. This fact was verified by visual examination and by color photographs during track formation.

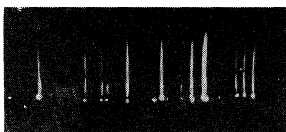
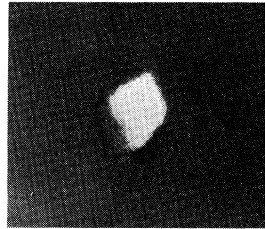
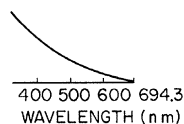


FIG. 10. Spectrum (vertical axis) vs track position (horizontal axis) of side-scattered light. A wavelength calibration curve is given to the right.



NO SAMPLE



NO TRACK



TRACK FORMED

FIG. 11. Track formation looking upstream. The exit beam divergence angle increases when a track is formed.

#### FORWARD-SCATTERED LIGHT

The divergence angle of the light transmitted through a sample increases when a track is formed. Photographs of this effect are shown in Fig. 11. The lower photograph of the forward-scattered light shows a large increase in the beam divergence angle (limited by the camera aperture) only when a track is formed in the sample.

#### Polarization

If the forward-scattered light is photographed through a linear polarizer, one finds that the light is polarized as a function of direction as shown in Fig. 12. Note that the forward-scattered light is strongly polarized in the vertical and horizontal directions. This effect is shown most dramatically in the bottom photograph, made with the polarizer perpendicular to the plane of polarization of the laser radiation.

The polarization results suggest reflections from a smooth dielectric interface during beam trapping.

#### Angle of the Forward-Scattered Light

The angle of the forward-scattered light was measured to be 0.8 rad in fused silica. This was done by photographing the light over a full angle of 1.4 rad while stopping the small-angle light. For comparison, a  $2\text{-}\mu\text{m}$ -diam object has a diffraction-limited angle

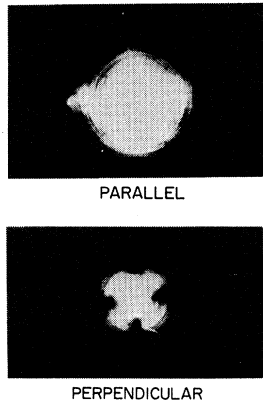


FIG. 12. Track formation looking upstream through a linear polarizer. The polarizer is either parallel or perpendicular to the polarization of the incident laser beam.

$$\theta = \frac{2.44\lambda}{D} = \frac{2.44 \times 0.7 \mu\text{m}}{2 \mu\text{m}} = 0.86 \text{ rad.}$$

We account for the large forward-scatter angle by assuming that the light is trapped or focused into a filament a few microns in diameter. As the light leaves the filament, it therefore spreads by diffraction to a large angle. This assumption agrees with the track diameter measurement.

We photographed the end of the filament, using the apparatus in Fig. 13. A track was formed so that it ran all the way to the exit face of the sample. A stop was placed in the center of the rear surface of a microscope objective to block out a circle equal to one-half the size of the objective. This stop was 4 mm in diameter and was twice the unfocused beam diameter.

A dense flint glass sample with a low damage threshold, and a 5.4-cm focusing lens (which would normally cause the exit beam to diverge at a wide angle) were chosen to keep the energy density of the light at the microscope objective to a minimum and thus avoid damaging the objective.

The data recorded are shown in Fig. 14. The upper photograph was taken while a track was formed. It shows a small illuminated region about 3 μm in diameter. The lower photograph shows

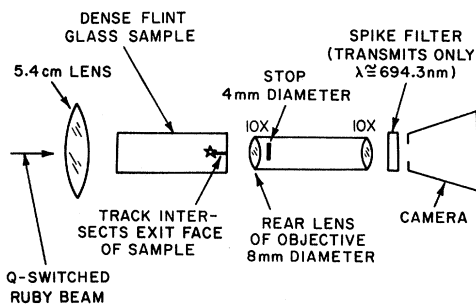


FIG. 13. Microphotography apparatus for recording track formation and exit surface pitting.

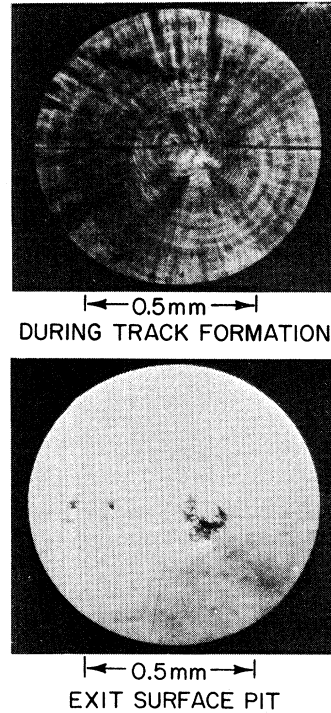


FIG. 14. Microphotographs of the sample exit face during and after track formation.

the damaged exit surface of the sample afterwards.

This measurement of 3 μm with a 5.4-cm lens is in good agreement with the previous track diameter measurement of 1.3 to 3.6 μm for tracks in dense flint glass formed with a 46-cm lens.

To conclude, this experiment demonstrates that the light is focused into a filament a few microns in diameter by the track formation phenomenon itself. It also indicates that the track diameter is only weakly dependent on the focal length of the lens used to create the track.

Time Dependence of the Forward-Transmitted Light

The time dependence of the small-angle (<0.04 rad) forward-transmitted light was measured for dense flint glass. Light was focused in the sample with a 5.4-cm lens, passed through an aperture and detected with an ITT F4000 photodiode. A typical oscilloscope tracing is shown in Fig. 15(a). The sudden drop of the forward-transmitted light can be interpreted as occurring when the light is suddenly focused into the track region of a few microns diameter. (The drop-below axis is an artifact due to circuit ringing.)

The time dependence of the large-angle forward-transmitted light was measured for the same SFS-5 sample and focusing lens. The light was collected over an angle of 1.4 rad while a stop blocked the small-angle light over an angle of 0.06 rad. A

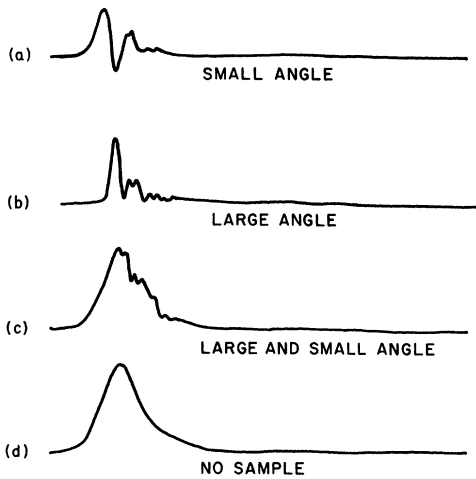


FIG. 15. Intensity of forward-transmitted light. The full width at half-maximum of the lowest trace is 55 nsec.

typical oscilloscope tracing is shown in Fig. 15(b). Here the sudden rise can be interpreted as occurring when the light is focused into the track region.

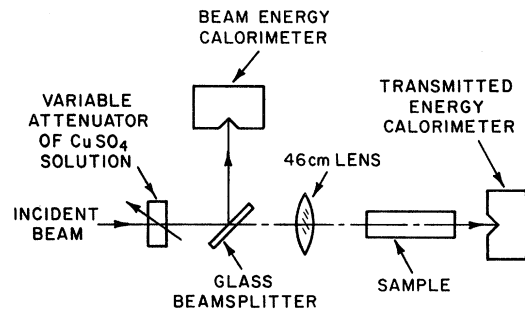


FIG. 16. Apparatus for measuring energy loss during track formation.

As a check, the small-angle (0.06-rad) stop was removed and all of the forward-transmitted light was recorded during track formation, and again when the sample was removed. These recordings are shown in Figs. 15(c) and 15(d), respectively. That they are quite similar is interpreted to mean that most of the forward-transmitted light is collected and that all other losses are small.

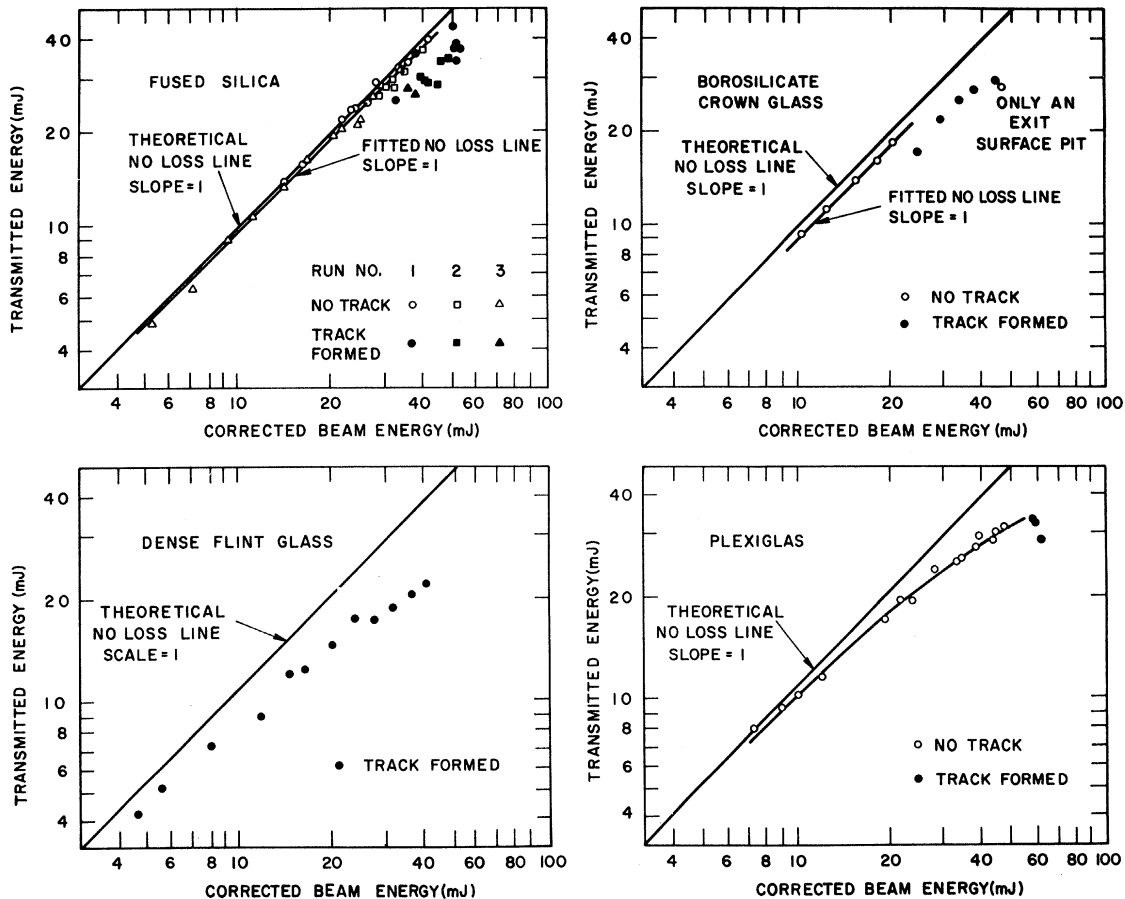


FIG. 17. Energy transmitted by four materials with and without track formation.

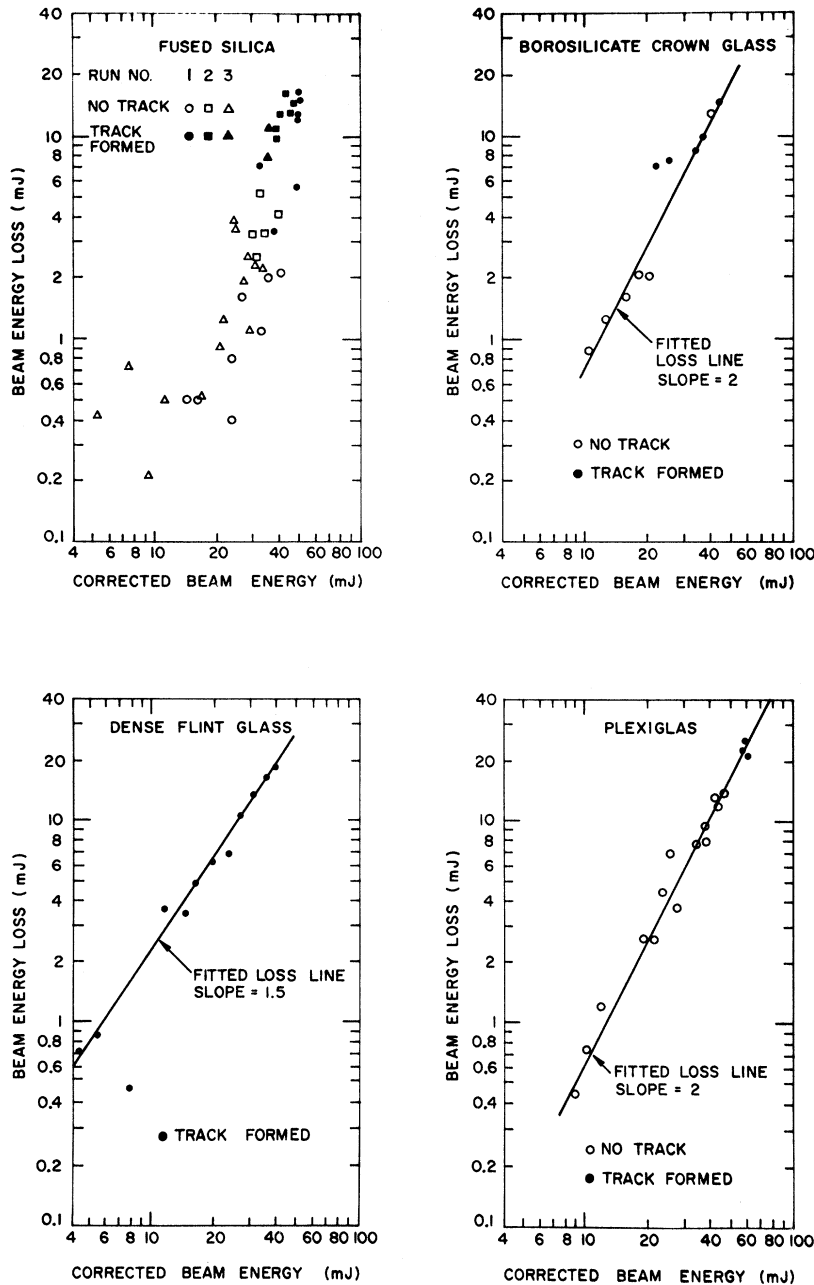


FIG. 18. Beam energy loss for four materials as a function of incident beam energy.

#### Forward-Transmitted Energy

We obtained information about the amount of energy involved in track formation by recording the transmitted energy and the incident beam energy simultaneously. The amount of energy removed from the beam sets the upper limit to the energy used in forming a track.

Two calorimeters were used in this experiment. They agreed to within  $\pm 2.5\%$  on individual trials, and to within better than  $1\%$  on an average basis.

The apparatus is depicted schematically in Fig.

16. The incident beam energy was varied by altering the concentration of the copper sulfate solution. We corrected the measured beam energy by subtracting calculated surface losses, so it would be the same as the measured transmitted energy in the absence of other loss mechanisms.

Sample materials were fused silica, borosilicate crown glass, dense flint glass, and Plexiglas (methylmethacrylate). The measured transmitted energy versus corrected beam energy is plotted in Fig. 17. The plot for fused silica is a composite of three runs made at different times. This plot

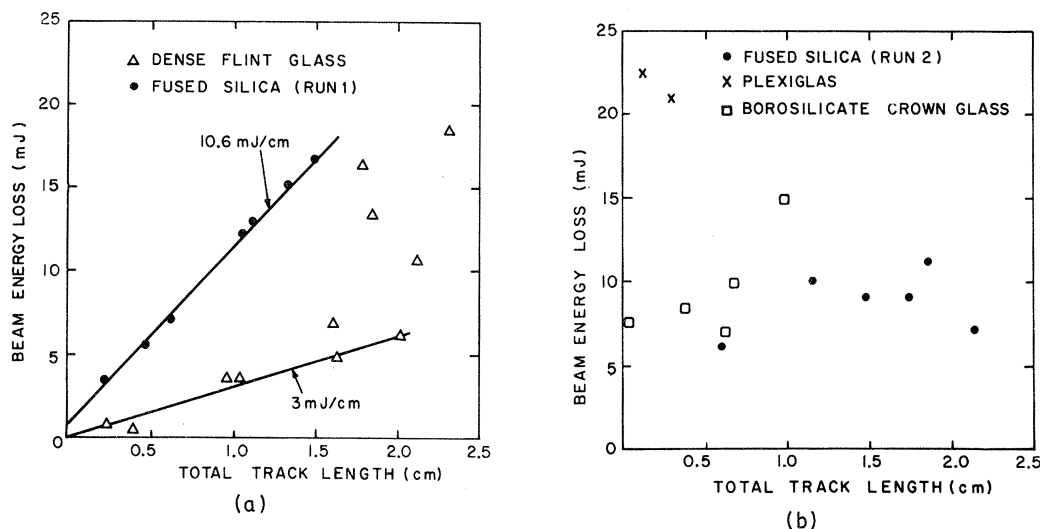


FIG. 19. Beam energy loss as a function of track length.

shows the best agreement between the no track points and the theoretical line representing no losses.

The beam energy loss was found by taking the difference between the corrected beam energy and the transmitted energy. This difference was plotted against the corrected beam energy on logarithmic graph paper in Fig. 18 for the four materials. The indication is that the beam energy loss depends on some power of the corrected beam energy. Borosilicate crown glass and Plexiglas were quite similar, the power being equal to 2. The noisiest graph was for fused silica because the losses were small when no damage occurred.

Suppose the beam energy loss were simply proportional to the track volume. Then, if the average track diameter stays constant, the length of the track will be proportional to the beam energy loss.

To test this hypothesis, for each trial we added up the lengths of all the track sections. When the beam energy loss was plotted against the total track length in Fig. 19(a), a linear relationship was found for fused silica (run 1). Dense flint glass also showed a linear relationship for short tracks. All the other runs resulted in widely scattered points Fig. 19(b). For fused silica, 10.6 mJ are lost per centimeter of track length, and for dense flint glass, 3 mJ/cm. The beam energy loss per cubic centimeter of track volume is  $7.4 \times 10^5$  J/cm<sup>3</sup> for fused silica and  $0.5 \times 10^5$  J/cm<sup>3</sup> for dense flint glass using the average measured track diameters.

If all this beam energy loss  $\Delta E$  were due to absorption, the temperature rise  $\Delta T$  of the materials would be  $\Delta T = \Delta E/C$  where the specific heat  $C$  is 2 J/(°C cm<sup>3</sup>). For fused silica the temperature rise would be 370 000 °C, before dissipation from

the track volume.

Such a temperature is much too high for the kind of damage observed. If we assume instead that the fused silica reaches a temperature of 1720 °C, the softening point, then the fraction of the energy required to heat the material to this temperature is  $1720^\circ\text{C}/370\,000^\circ\text{C} = 0.46\%$ .

In other words, only  $\frac{1}{2}\%$  of the beam energy loss is required to raise the temperature of fused silica to its softening point. The remaining energy must be lost by other mechanisms.

#### BACK-SCATTERED (BRILLOUIN) LIGHT

Light was scattered in the back direction only when a track was formed in our experiments. We photographed the back-scattered light through a pellicle placed between the sample and the 46-cm lens. The left-hand photograph in Fig. 20 shows the sample end-face reflections when no track was formed. The end faces were not perpendicular to the incident beam nor were they parallel to each other. The right-hand photograph of the same figure shows these same end-face reflections plus an

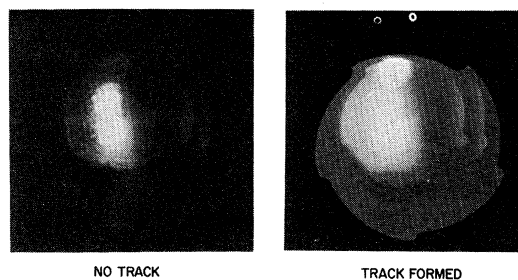


FIG. 20. Back-scattered light during track formation.

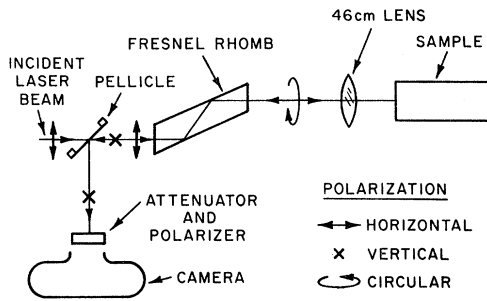


FIG. 21. Apparatus for observing back-scattered light during track formation by a circularly polarized laser pulse.

additional beam of light when a track was formed. Note that the diameter of the additional beam of light (the back-scattered beam) is approximately the same as the diameter of the reflected beams and hence is approximately the same as the diameter of the incident beam (not shown).

#### Polarization

By placing a polarizer between the camera and the pellicle we found that the back-scattered beam was linearly polarized in the same plane as the incident laser beam.

When the track was formed with a circularly polarized laser beam, the back-scattered beam was also circularly polarized. This experiment can be followed in detail by referring to Fig. 21. The horizontally polarized laser beam passes through the Fresnel Rhomb quarter wave retarder and becomes circularly polarized. If this light were reflected from a mirror and passed through the Rhomb again, it would become vertically polarized. This is exactly what was observed to occur when a track was formed. The back-scattered beam was vertically polarized at the camera after passing through the Rhomb. Thus it must have been circularly polarized as it left the sample entrance face.

The back-scattered light, therefore, completely

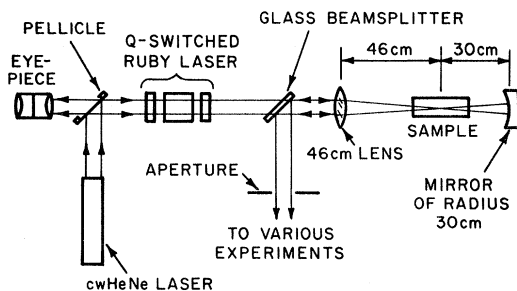


FIG. 22. Alignment apparatus for making the ruby-laser beam coincident with a He-Ne laser beam.

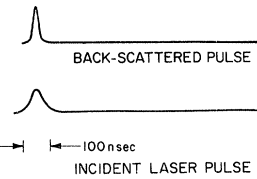


FIG. 23. Comparison of the back-scattered pulse intensity distribution with the incident laser pulse.

preserves the polarization of the incident beam.

#### Retrodirection

Another experiment determined that the back-scattered beam is retrodirected upon the incident beam. We used a cw He-Ne laser beam to simulate the incident beam and to predict the position of the back-scattered beam. We then found that the actual back-scattered beam was indeed coincident with the cw prediction.

The experimental apparatus used is depicted in Fig. 22. We used the He-Ne laser to align the Q-switched ruby-laser resonator by making the reflections from the resonator coincident on the cross hairs of an eyepiece. A portion of the He-Ne laser beam passes through the output mirror of the ruby-laser resonator. It is coincident with the Q-switched ruby-laser beam. The cw beam passes through the 46-cm lens and the sample and is returned by the spherical mirror so the beam returns to the cross hairs of the eyepiece. A portion of the return beam is sampled with a beam splitter and passed through an aperture. When we removed the spherical mirror and formed a track, the back-scattered beam passed through the same aperture. The back-scattered beam is therefore coincident with the Q-switched ruby-laser beam.

#### Pulse Duration

We determined the back-scattered pulse duration by placing a photomultiplier tube behind the aperture shown in Fig. 22.

The back-scattered pulse duration was found to be only 15–20 nsec when the laser pulse duration was 55 nsec. Typical pulses are compared in Fig. 23. Note that the back-scattered pulse rise time is faster than the laser-pulse rise time.

When tracks were formed in ruby and sapphire samples with the 5.4-cm lens, no back-scattered light was observed at all. This is in marked contrast to materials like fused silica, borosilicate crown glass, and dense flint glass, where the back-scattering threshold is the same as the track formation threshold.

#### Frequency Shift

We suspected that the back-scattered beam was Brillouin scattered. To test the supposition, we compared the frequencies of the incident and back-

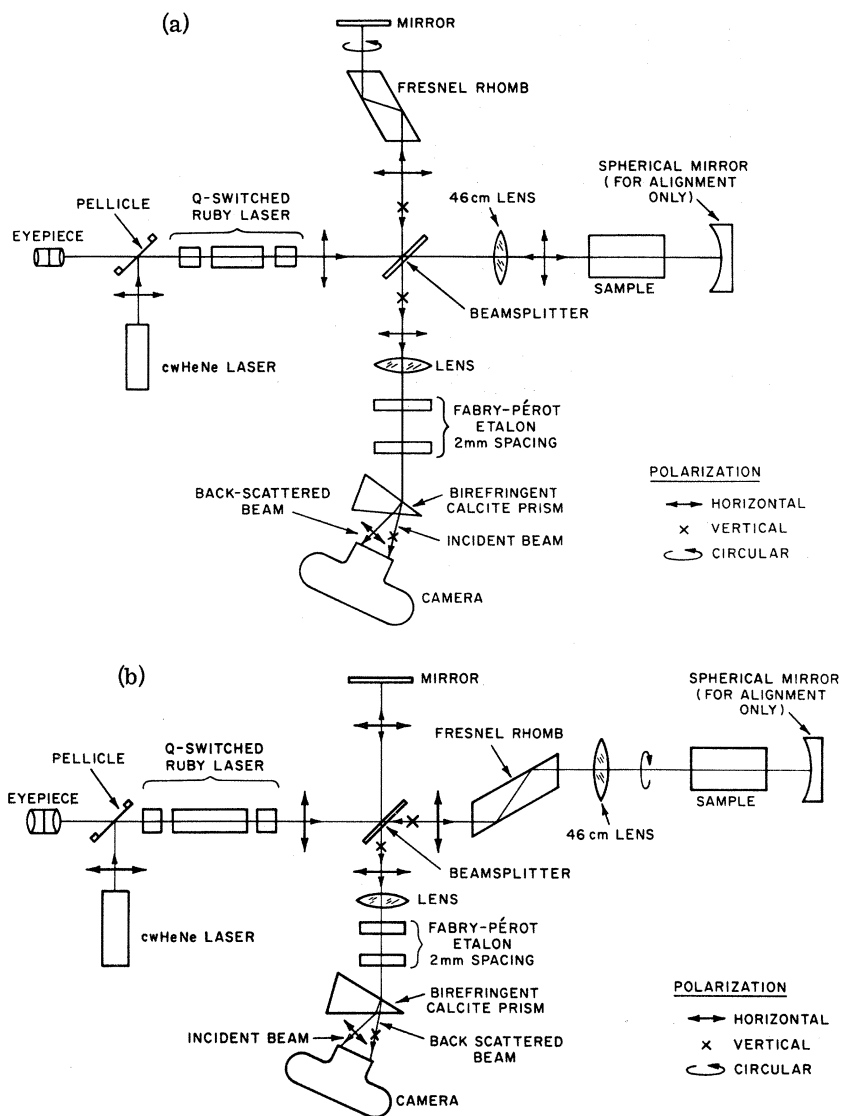


FIG. 24. Apparatus to separately record incident and back-scattered frequencies during track formation (a) by a linearly polarized laser pulse and (b) by a circularly polarized laser pulse.

scattered beams by simultaneously passing them through a Fabry-Perot etalon, separating them spatially, and photographing the ring patterns.

The experiment designed to do this is shown in Fig. 24(a). The cw laser and the spherical mirror are used only to simulate the Q-switched ruby-laser beam for alignment purposes. The spherical mirror was removed before track formation. For the linear-polarization case, the incident laser beam and the back-scattered beam are horizontally polarized. The beam splitter sends a sample of the back-scattered beam through the etalon. The same beam splitter samples the incident beam. By passing through the Fresnel Rhomb twice, the polarization plane of the sampled incident beam is rotated  $90^\circ$ . It is directed through the etalon coincidentally with the sampled back-scattered beam. After passing through the etalon both beams are polarized at

right angles to each other. They are spatially separated by a birefringent calcite prism. The fringe pattern of each beam is then photographed during track formation.

A similar arrangement is shown in Fig. 24(b) for tracks formed by a circularly polarized beam. The polarizations of the two beams are reversed from the previous case.

The typical photographs in Fig. 25 clearly show a frequency shift. Each half of the composite photograph shows some leakage light of the opposite polarization. The prism has distorted the ring pattern except in the vertical direction, where the photographs are divided.

The frequencies are compared by measuring the ring diameters on the enlarged photograph in the vertical (no distortion) direction for both the back-scattered and the incident beams.

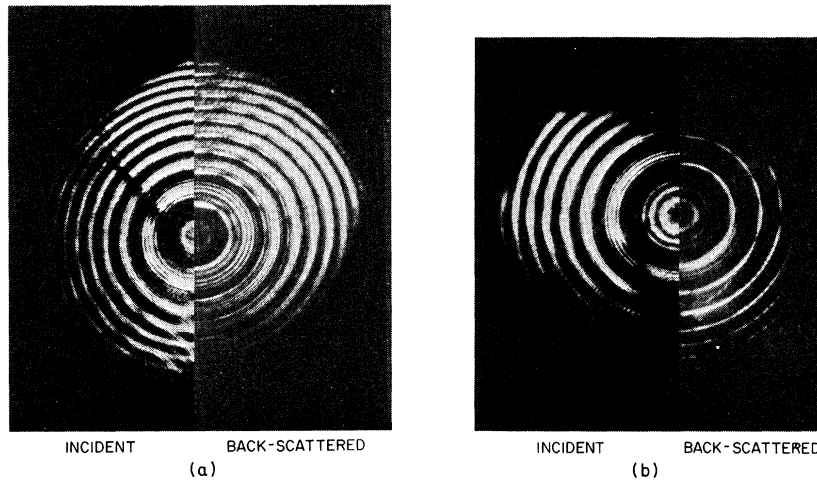


FIG. 25. Frequency shift for track formation (a) by a linearly polarized laser pulse and (b) by a circularly polarized laser pulse.

A scale factor  $k$  is required to adjust the measured diameter  $D_m$  of a ring on the enlargement to the diameter  $D$  that ring would have on the rear face of the etalon, such that

$$D = k D_m \quad (1)$$

The scale factor  $k$  is computed by noting that the path length through the etalon to the ring of diameter  $D$  must be an integral number of half-wavelengths or

$$d / \cos \alpha = N \lambda / 2, \quad (2)$$

where

$$\tan \alpha = D / 2d$$

and  $d$  is the etalon spacing,  $\alpha$  is the half-angle of ring of diameter  $D$ , and  $N$  is the number of half-wavelengths. By simultaneously solving the pair of equations similar to Eq. (2) that result for two rings of the same wavelength but adjacent order, the scale factor  $k$  is found to be

$$k^2 = 4d\lambda / (D_{2m}^2 - D_{1m}^2),$$

where  $D_{1m}$  and  $D_{2m}$  are the measured diameters of rings of the same wavelength and adjacent orders.

By a similar process of solving the pair of equations that result for two rings of *different* wavelength but the *same* order, the frequency shift  $\Delta\nu$  in wave numbers is computed to be

$$\Delta\nu = (k^2 / 8\lambda d^2) [D_{1m}^2(\lambda_a) - D_{1m}^2(\lambda_b)], \quad (3)$$

where  $D_{1m}(\lambda_a)$  and  $D_{1m}(\lambda_b)$  are the diameter of rings of different wavelengths but the same order, as measured on the enlargement.

When this computation was made, an identical frequency shift,  $0.82 \text{ cm}^{-1}$  (where frequency is measured in wave-number units), was found for both the linearly and the circularly polarized back-scattered beams.

For Brillouin scattering the frequency shift  $\Delta\nu = 2nv/\lambda c$ . Using  $n = 1.455$  for fused silica, we obtain  $v = 5900 \text{ m/sec}$ . This may be compared with the value  $5980 \text{ m/sec}$  calculated in Table I.

#### Energy Content

To gauge the relative importance of Brillouin scattering in track formation, we measured the energy content of the back-scattered beam.

First we tried to measure the back-scattered beam energy by placing a calorimeter behind the aperture of Fig. 22. This experiment gave no reading because the calorimeter was not sensitive enough to respond to the fraction of the back-scattered beam sampled by the beam splitter. The minimum energy which could have been detected by the calorimeter corresponded to 1 mJ in the entire back-scattered beam.

A second measurement was therefore attempted in which 100% of the back-scattered beam was sampled. We used the Fresnel Rhomb to put the planes of polarization of the incident and back-scattered beams at right angles to each other, and a birefringent calcite prism to separate them spatially (Fig. 26).

This experiment also gave no reading for fused silica. The back-scattered beam was attenuated by the additional reflection losses to below the threshold value for track formation. We therefore tried the experiment on dense flint glass, which has a lower threshold. When 57 mJ were incident at the front face of the sample, 1 mJ was back scattered. The back-scattered energy was only about 10% of the beam energy loss.

Because the back-scattered energy is such a small fraction of the total beam energy loss, Brillouin scattering is probably not an important aspect of track formation.

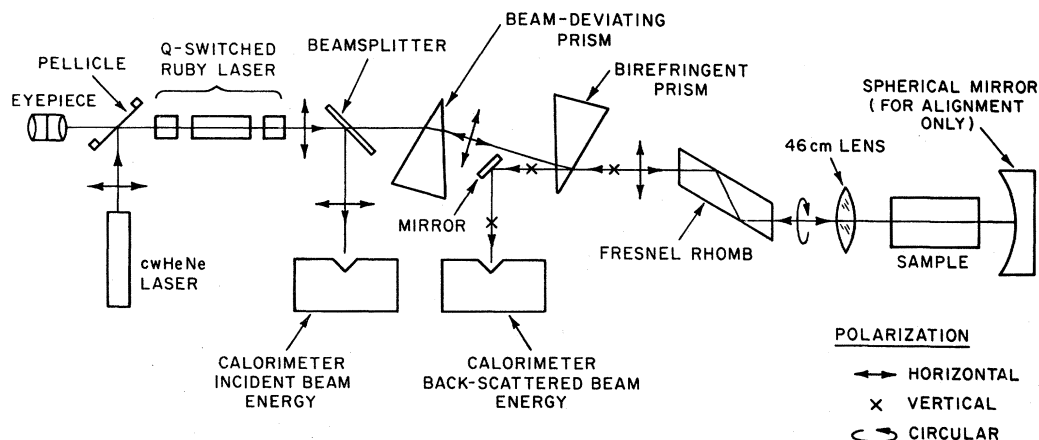


FIG. 26. Apparatus for measuring the energy of the back-scattered light.

### CONCLUSIONS

The data presented here show conclusively that the laser tracks formed in optical materials are merely the "fossil" record of a trapped filament from a high-power  $Q$ -switched laser beam.

The facts that the light is seen to emanate from the track core, and that the track aspect ratio is extremely large, are the critical points in support of beam trapping. These two facts are mutually exclusive unless beam trapping is assumed.

Other evidence, such as the angular distribution of the transmitted light as a function of time and the polarization of the transmitted light, also support the beam trapping concept.

Beam trapping is feasible on an energy basis. The energy measurements show that the maximum available energy is large relative to the energy required to create the track.

The threshold measurements are interesting in their own right for their practical value. But they are also the test which any proposed theory of track formation must meet.

### ACKNOWLEDGMENTS

I wish to thank John Atwood and Paul Lee for their guidance with experimental work and to Edwin Kerr for helping to bring this manuscript to fruition.

\*Research sponsored by U. S. Army Electronics Command, Fort Monmouth.

<sup>1</sup>M. Hercher, J. Opt. Soc. Am. 54, 563 (1964).

<sup>2</sup>T. Li and S. D. Sims, Appl. Opt. 1, 325 (1962).

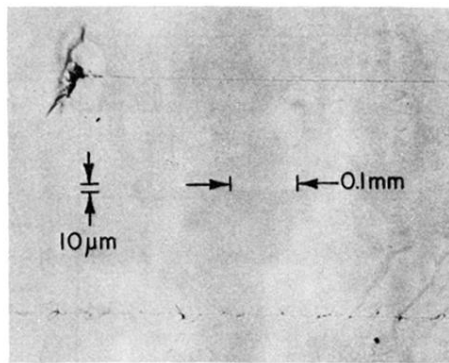


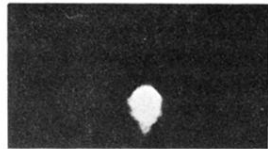
FIG. 1. Two typical filamentary tracks with damage stars.



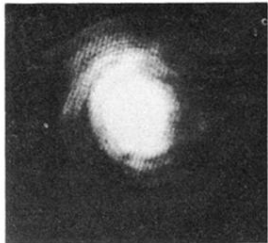
FIG. 10. Spectrum (vertical axis) vs track position (horizontal axis) of side-scattered light. A wavelength calibration curve is given to the right.



NO SAMPLE

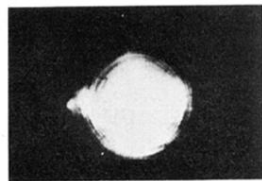


NO TRACK

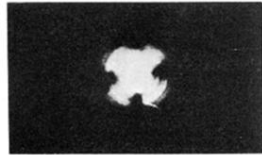


TRACK FORMED

FIG. 11. Track formation looking upstream. The exit beam divergence angle increases when a track is formed.

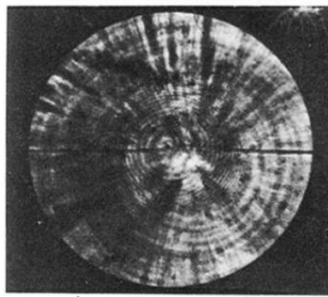


PARALLEL



PERPENDICULAR

FIG. 12. Track formation looking upstream through a linear polarizer. The polarizer is either parallel or perpendicular to the polarization of the incident laser beam.



←0.5mm→  
DURING TRACK FORMATION



←0.5mm→  
EXIT SURFACE PIT

FIG. 14. Microphotographs of the sample exit face during and after track formation.

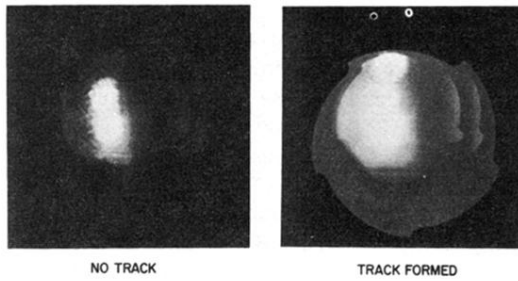
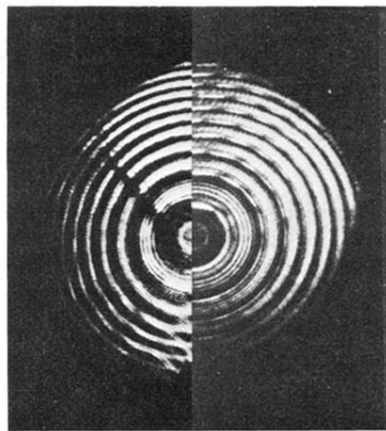


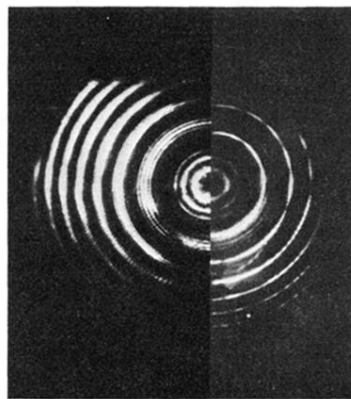
FIG. 20. Back-scattered light during track formation.



INCIDENT

BACK-SCATTERED

(a)



INCIDENT

BACK-SCATTERED

(b)

FIG. 25. Frequency shift for track formation (a) by a linearly polarized laser pulse and (b) by a circularly polarized laser pulse.

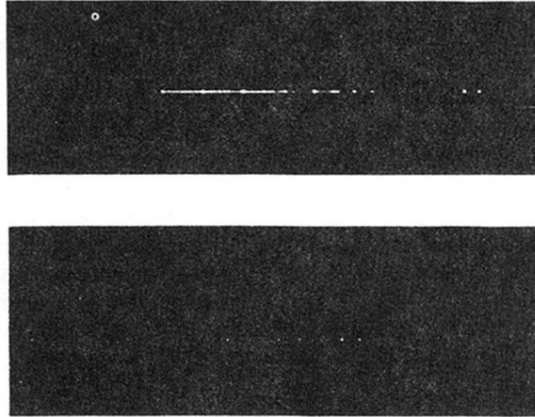
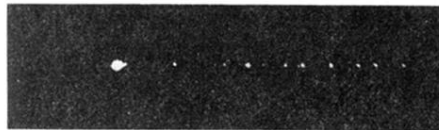


FIG. 6. Side-scattered white light (upper photo) and laser light (lower photo) during track formation. The laser pulse was incident from the left-hand side in each photo.

DURING



AFTER



FIG. 7. Track photographs during (upper) and after (lower) formation. The laser pulse was incident from the left-hand side. The upper photo shows laser light only, as the side-scattered white light was blocked by a 694.3-nm spike filter. (Microscope cross hairs and dust in the lower photo should be ignored.)